

Boundary and Interior Layers in Turbulent Thermal Convection *

Olga Shishkina & Claus Wagner

DLR - Institute for Aerodynamics and Flow Technology,
Bunsenstrasse 10, 37073 Göttingen, Germany
Olga.Shishkina@dlr.de, Claus.Wagner@dlr.de

1. Introduction

Turbulent convection of fluids heated from below and cooled from above, which is known in literature as Rayleigh–Bénard convection (RBC) [1]–[2], is one of the classical problems in fluid dynamics. The most interesting examples of this process are convection in atmospheres, in oceans, on surfaces of stars.

There are three main parameters characterizing fluid motion in RBC: the Rayleigh number $Ra = \alpha g H^3 \Delta T / (\kappa \nu)$, the Prandtl number $Pr = \nu / \kappa$ and the aspect ratio of the container $\Gamma = D / H$. Here α denotes the thermal expansion coefficient, g the gravitational acceleration, ΔT the temperature difference between the bottom and the top plates, κ the thermal diffusivity, ν the kinematic viscosity and H the height and D the diameter of the Rayleigh cell. Numerous scientific and industrial problems require a better understanding of the physics of Rayleigh–Bénard convection for the Rayleigh numbers up to 10^{20} and large aspect ratios.

The diffusion coefficients in the governing Navier–Stokes and the heat equations, which are inversely proportional to the square root of Ra , are very small. (For example, for $10^5 \leq Ra \leq 10^9$, $Pr = 0.7$ and $\Gamma = 10$ the diffusion coefficient in the Navier–Stokes equation varies from $8.36 \cdot 10^{-5}$ to $8.36 \cdot 10^{-7}$.) Therefore the solutions – both the temperature and the velocity fields – have very thin boundary layers near the horizontal walls and interior layers which are recognized as large coherent structures in visualizations of the flows.

Experimental studies of RBC show that above but close to the onset of convection ($Ra \approx 1.7 \times 10^3$) visible flow patterns reflect straight rolls with certain defects induced by the sidewalls [1]. Further above the onset for $Pr \leq 1$ the spiral–defect chaos evolves [3] and for $Ra \approx 6.8 \times 10^3$ hexagon patterns occur [4]. Both types of polygon convection cells – those with rising (l-cells) and those with descending (g-cells) motion in the center – can coexist with the spirals [5]. When the Rayleigh number exceeds a value of order 10^4 the spoke patterns [6] evolve, which tend to be nearly stationary for lower Ra close to the onset of this type of convection and appear chaotically when the Rayleigh number exceeds 10^5 . A further increase of Ra tears off unstable spokes to form more independent large scale flow structures, which are called thermal plumes and are generated from the horizontal thermal boundary layers and driven by buoyancy. The thermal plumes play an important role in the moderate-Rayleigh-number regime that begins at $Ra = 10^5$. Close to $Ra = 10^8$ the large-scale circulation initiated by thermal plumes develops [7].

The thermal boundary layers, the borders of coherent interior flow structures and the turbulent background are indicated, respectively, by high, moderate and small values of the temperature gradient norm and, hence, by large, moderate and small values of the thermal dissipation rate. In contrast to experimental studies of thermal convection, in which only restricted information is available, numerical simulations enable to investigate quantitatively the boundary and interior layers and turbulent background, since they provide all details of the flow fields needed to calculate the dissipation rates.

*The work is supported by Deutsche Forschungsgemeinschaft (DFG) under the contract WA 1510-1

To investigate boundary and interior layers which occur in the moderate-Rayleigh-number regime of turbulent Rayleigh–Bénard convection in wide cylindrical containers filled with air we conducted direct numerical (DNS) and Large-Eddy (LES) simulations of RBC for $10^5 \leq Ra \leq 10^8$ and $\Gamma = 5$ and 10 .

2. Governing equations and the numerical method

The governing dimensionless equations for Rayleigh–Bénard problem in Boussinesq approximation can be written in cylindrical coordinates (z, r, φ) as follows

$$\mathbf{u}_t + \mathbf{u} \cdot \nabla \mathbf{u} + \nabla p = \Gamma^{-3/2} Ra^{-1/2} Pr^{1/2} \Delta \mathbf{u} + T \mathbf{z}, \quad (1)$$

$$T_t + \mathbf{u} \cdot \nabla T = \Gamma^{-3/2} Ra^{-1/2} Pr^{-1/2} \Delta T, \quad (2)$$

$$\nabla \cdot \mathbf{u} = 0, \quad (3)$$

where \mathbf{u} is the velocity vector, T the temperature, \mathbf{u}_t and T_t their time derivatives, p the pressure. The dimensionless temperature varies between $+0.5$ at the bottom plate to -0.5 at the top plate. On the solid walls $\partial T / \partial r = 0$ and the velocity field vanishes according to the impermeability and no-slip conditions. Note that in cylindrical coordinates operators ∇ , $(\nabla \cdot)$ and Δ read

$$\begin{aligned} \nabla a \equiv \text{grad } a &= \left(\frac{\partial a}{\partial z}, \frac{1}{r} \frac{\partial a}{\partial \varphi}, \frac{\partial a}{\partial r} \right), & \nabla \cdot \mathbf{a} \equiv \text{div } \mathbf{a} &= \frac{\partial a_z}{\partial z} + \frac{1}{r} \left(\frac{\partial a_\varphi}{\partial \varphi} + a_r \right) + \frac{\partial a_r}{\partial r}, \\ \Delta a \equiv \nabla \cdot \nabla a &= \frac{\partial^2 a}{\partial z^2} + \frac{1}{r} \frac{\partial a}{\partial r} + \frac{1}{r^2} \frac{\partial^2 a}{\partial \varphi^2} + \frac{\partial^2 a}{\partial r^2}, \end{aligned}$$

where $\mathbf{a} = (a_z, a_\varphi, a_r)$ is any vector-function in coordinates (z, φ, r) .

Turbulent Rayleigh–Bénard convection in cylindrical containers of the aspect ratios $\Gamma = 10$ and $\Gamma = 5$ for $Pr = 0.7$ was studied numerically by means of DNS for Rayleigh numbers from 10^5 to 10^7 and LES utilizing the tensor-diffusivity model [8] together with the top-hat filtering for $Ra = 10^8$. The simulations were performed with the fourth order accurate finite volume method developed for solving (1) – (3) in cylindrical coordinates on staggered non-equidistant grids. For the description of the numerical method used in the simulations we refer to [9].

3. Thermal boundary layers and their resolution

In turbulent RBC there are two thermal boundary layers near the horizontal walls. In the vicinity of these walls the mean temperature profiles $\hat{T}(z) = \langle T \rangle_{t, S_z}$, where $\langle \cdot \rangle_{t, S_z}$ denotes averaging in time and over any horizontal plane S_z , change dramatically and stay almost near zero in the

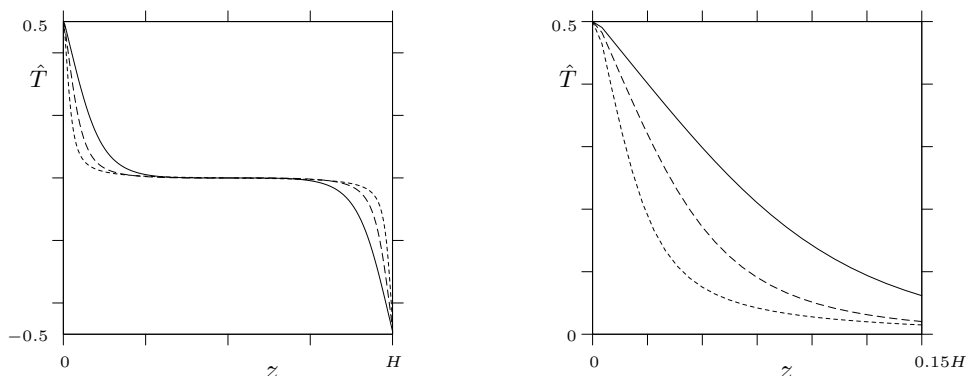


Figure 1: Averaged in time and in the φ - and r -directions temperatures $\hat{T}(z)$ (left) and its close-up view (right) for $Ra = 10^5$ (—), $Ra = 10^6$ (---) and $Ra = 10^7$ (- - -) and $\Gamma = 10$.

bulk. The temperature profiles given Fig.1 reflect that the thickness of the thermal boundary layer, which is defined formally as $\lambda = H/(2Nu)$, decreases with growth of the Rayleigh number.

Further, in [10] it was proven that the ratio of the area averaged (over the top or the bottom plates) to the volume averaged thermal dissipation rate

$$\epsilon_\theta = \Gamma^{-3/2} Ra^{-1/2} Pr^{-1/2} (\nabla T)^2 \quad (4)$$

is greater than or equal to the Nusselt number

$$Nu = \Gamma^{1/2} Ra^{1/2} Pr^{1/2} \langle u_z T \rangle_{t,S} - \Gamma^{-1} \left\langle \frac{\partial T}{\partial z} \right\rangle_{t,S}, \quad (5)$$

which is larger than 1 for all Ra , Pr and Γ . (Here u_z is the component of the velocity field in the vertical direction z .) Since the mean heat flux, which is expressed by the Nusselt number, increases with the Rayleigh number, this ratio also increases with Ra . The facts that the largest values of ϵ_θ occur generally in the thermal boundary layers near the horizontal walls and that the thickness of the thermal boundary layers decreases with increasing Rayleigh number require to develop a proper mesh generation mechanism to control the thermal boundary layers resolution.

In practice, to simulate turbulent Rayleigh–Bénard convection the following mesh generation technique is used. To resolve all relevant turbulent scales the mean mesh width in the bulk is chosen of the order of the Kolmogorov scale which can be estimated as follows [11]

$$h(Ra) \approx \pi \Gamma^{-1} Pr^{1/2} (Nu - 1)^{-1/4} Ra^{-1/4}. \quad (6)$$

This mean mesh width is turned to account to construct an equidistant mesh. Sometimes a certain number of additional nodes are implanted near the horizontal walls, where the boundary layers are expected, as it was done in DNS by Verzicco and Camussi [12]. This manner of mesh generation is acceptable for considerably low Rayleigh numbers and low aspect ratios Γ of the Rayleigh cell. For high-Rayleigh-number and high-aspect-ratio cases an adaptive mesh generation method is required.

4. Adaptive mesh generation for turbulent RBC simulation

Generally, strategies for solution-adapted mesh construction are based either on a priori or on a posteriori information about the solution. Although the methods of the first type [13], [14] can produce excellent meshes, for complicated problems such as turbulent Rayleigh–Bénard convection this a priori information is usually not provided. Among the methods which use a posteriori information the most effective ones are grid equidistribution methods [15], [16] and adaptive mesh refinement methods [17], [18]. The former use monitor functions for better distribution of the nodes and the latter start with very coarse meshes and use error indicators for their iterative refinement. Since turbulence simulations are impossible on very coarse meshes at all, the grid equidistribution approach was chosen to construct an effective mesh generation algorithm which could detect the boundary layers and produce appropriate meshes for their resolution.

In turbulent Rayleigh–Bénard convection for low Prandtl numbers horizontal thermal boundary layers are thinner than kinetic boundary layers. Therefore the temperature profiles must determine the distribution of the mesh nodes. Apart from this, the desired meshes must be structured and stationary, i.e. not variable in time, due to the following reasons. The meshes used in the DNS of fully turbulent three-dimensional convection are rather large and consist of $10^7 - 10^{11}$ nodes, since the mean mesh width in the bulk must be of the order of the Kolmogorov scale. Consequently the three-dimensional Poisson equation which couples the pressure and the velocity field has also a huge number of unknowns and thus must be solved by one of the fast

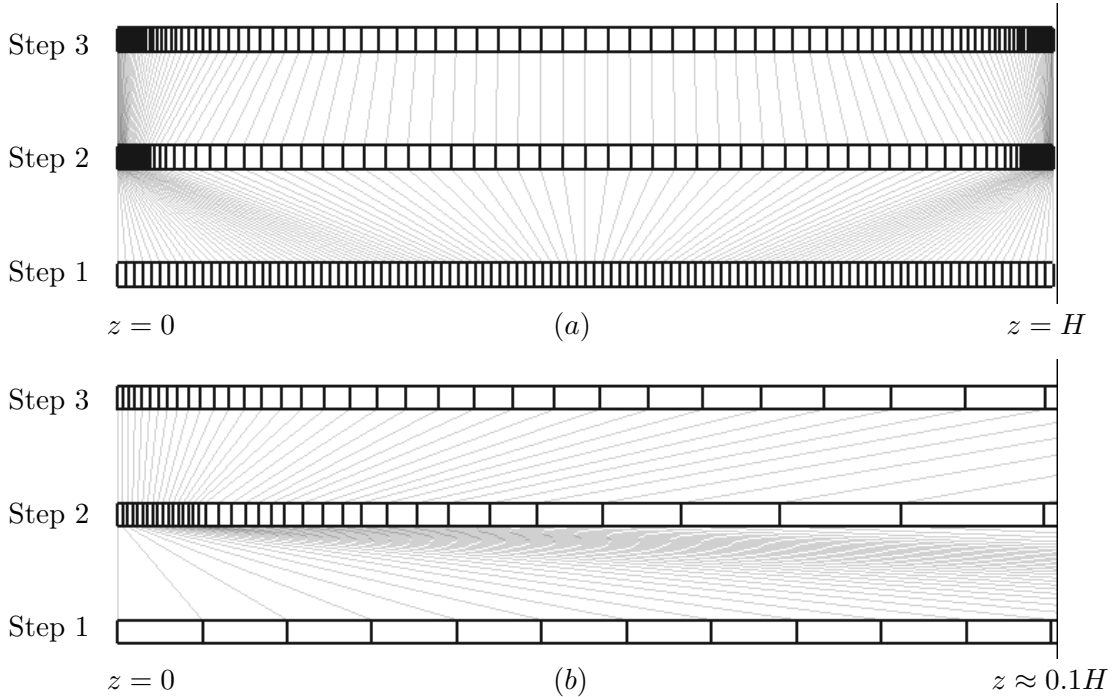


Figure 2: (a) Three steps of adaptive mesh generation, (b) close-up view of (a).

Poisson solvers that work on structured grids only. From the other hand, an accurate approximation of the solution due to the moving in time mesh with large number of nodes could be over time-consuming.

To simulate turbulent Rayleigh–Bénard convection an algorithm for adaptive mesh construction, which is based on equidistribution of the mean temperature profiles computed in the vertical z -direction on auxiliary (equidistant) meshes, was developed. The algorithm works in three steps.

In the first step a rough solution of the system (1) – (3) is found on an auxiliary mesh which is equidistant in the vertical z -direction. Averaging the temperature in time and also in the φ - and r -directions gives the temperature profile – a one-dimensional function $\hat{T}(z)$ (see Fig.1). An equidistant mesh of 110 intervals in the z -direction, which was used in our simulations for the case $Ra = 10^5$, $\Gamma = 10$, corresponds to Step 1 in Fig.2.

In the second step for a non-negative monitor function $M(z)$,

$$M(z) = \sqrt{1 + \left(d\hat{T}(z)/dz \right)^2}, \quad (7)$$

we find the points $\{z_k\}$, $k = 1, \dots, N_z$, which equidistribute $M(z)$ as follows

$$\int_{z_{k-1}}^{z_k} M(z) dz = \frac{1}{N_z} \int_0^H M(z) dz.$$

Then the mesh is checked. Each cell must be smaller than the Kolmogorov scale $h(Ra)$ (6) to resolve all turbulent scales. If the constructed mesh is too coarse, the number of nodes N_z is increased and the second step is repeated. In our test case this mesh is marked as "Step 2" in Fig.2 and is fine enough to resolve all relevant turbulent scales, since the mean mesh width $h_{DNS} = \max_i (\Delta z_i r_i \Delta \varphi_i \Delta r_i)^{1/3}$ is smaller than the Kolmogorov scale $h(Ra)$ for all considered Rayleigh numbers. In particular, for the mesh with 110, 192 and 512 intervals in the vertical z -, azimuthal φ - and radial r -directions, respectively, we get $h(10^5) = 4.37 \times 10^{-2}$, $h(10^6) = 1.98 \times 10^{-2}$ and $h(10^7) = 9.20 \times 10^{-3}$, while $h_{DNS} = 6.54 \times 10^{-3}$. This mesh is

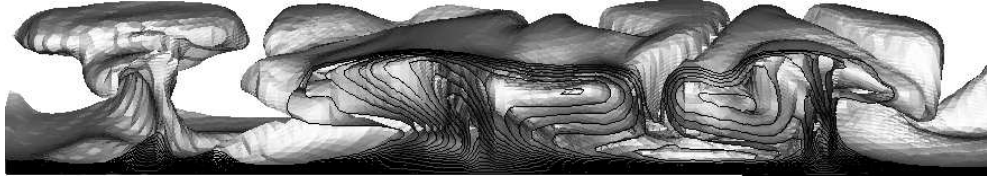


Figure 3: Hot thermal plumes visualized with 20 isotherms for $T \in [0, 0.5]$ in a subdomain of width $0.25R$, DNS for $Ra = 10^5$, $Pr = 0.7$, $\Gamma = 10$.

solution-adapted, but has the only one disadvantage: some intervals are more than 40% large than their neighbours and this irregularity can destabilize the simulations.

In the third step the hyperbolic tangent algorithm by Thompson [19] is used to make the mesh smoother. This algorithm provides a smooth distribution of the nodes on the interval $[0; 1]$, using the following incoming data: the number of the nodes and the sizes of the first and the last subinterval. The final mesh consists of $N_z = 110$ finite volumes in the z -direction (the same value was in the auxiliary mesh), is solution-adapted, and its neighbour intervals differs in size not more than 7%. This resulting mesh for the case $Ra = 10^5$, $\Gamma = 10$ corresponds to "Step 3" in Fig.2.

5. Thermal interior layers and their extraction

In turbulent RBC for moderate Rayleigh numbers ($10^5 \leq Ra \leq 10^8$) the thermal interior layers, i.e. plumes, take usually a mushroom-like form (see Fig. 3). In Fig. 4 instantaneous temperature fields obtained for different Rayleigh numbers are presented in (φ, r) -planes located close to the heated bottom plate. Additionally, snapshots of the temperature field for $Ra = 10^5$ in vertical planes are shown in Fig. 5 to illustrate the complexity of the flow structures which are generated in turbulent Rayleigh–Bénard convection for moderate Rayleigh numbers.

The temperature fields in the (φ, r) -plane located close to the heated bottom or cooled top plate reflect large scale structures denoted as the roots of the thermal plumes [10]. These roots become thinner and their number increases with the Rayleigh number. With growing Rayleigh number the thermal plumes start to cluster and the mean distance between the zones of clustered plumes increases.

The hot (cold) plumes, which are generated in the lower hot (upper cold) thermal boundary layer and driven by buoyancy, enter the upper cold (lower hot) thermal boundary layer. Due to the wall effect in the upper cold (lower hot) thermal boundary layer the hot (cold) fluid moves predominantly from the centres of the hot (cold) plume caps towards their borders and pushes away the cold (hot) fluid, which is channelized to form the roots of cold (hot) plumes. In the bulk region but still close to the top (bottom) boundary layer the fluid moves mainly through the roots towards the stems of the cold (hot) plumes. The stems of the plumes are generated at the intersections of the roots. In the bulk the fluid moves generally through the stems towards the caps of the plumes. The cold and hot plumes look similar, but they settle upside down.

Although the thermal plumes are visible in experiments and can be detected intuitively on the snapshots of the temperature fields produced in numerical simulations, methods for thermal plumes extraction and analysis of coherent flow patterns are required. The straightforward way to extract thermal interior layers – is to use the thermal dissipation rates ϵ_θ (4), large values of which indicate the thermal boundary layers and the borders of the thermal plumes. To separate visually hot and cold thermal plumes one can also use the function

$$C(T, \epsilon_\theta) = T\epsilon_\theta,$$

which is positive or negative, respectively, in warm ($T > 0$) or cold ($T < 0$) parts of the fluid

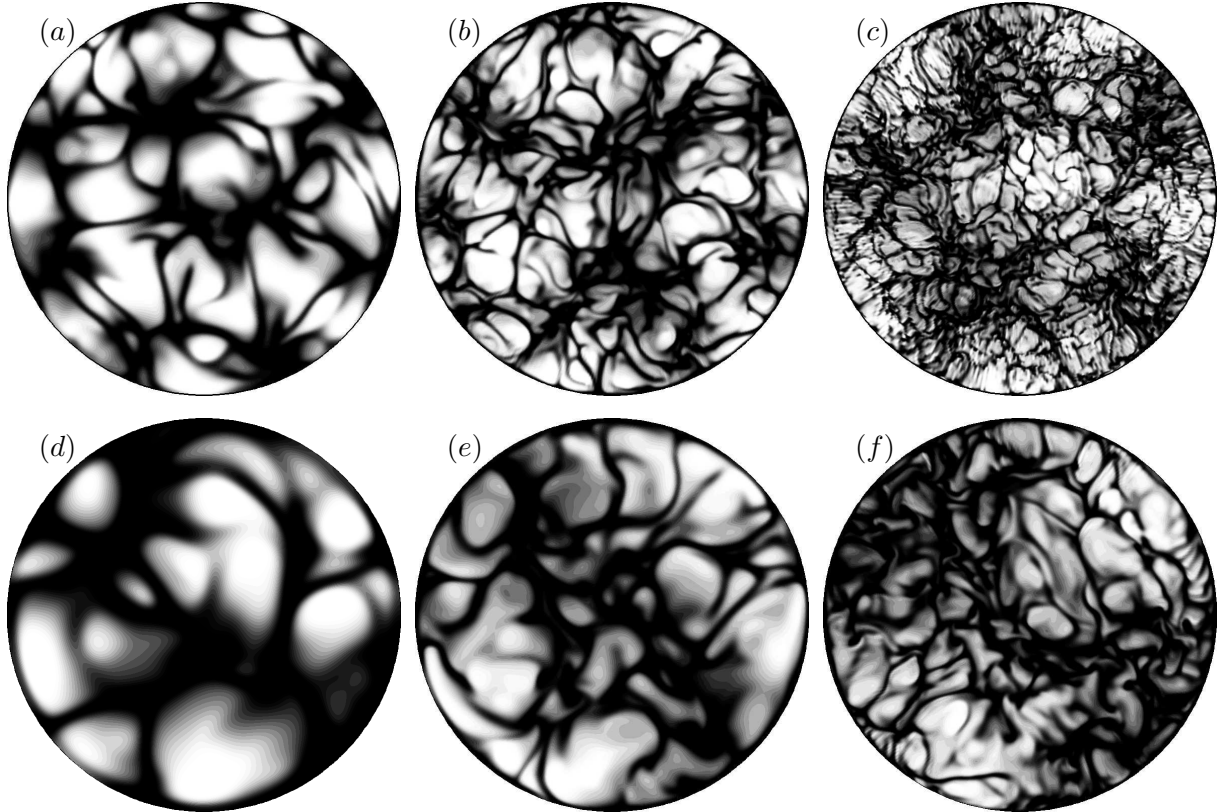


Figure 4: Snapshots of the temperature for $z = H/(2Nu)$, $\Gamma = 10$ (a, b, c), $\Gamma = 5$ (d, e, f) and $Ra = 10^5$ (a, d), $Ra = 10^6$ (b, e), $Ra = 10^7$ (c, f). Colour scale spreads from white (negative values) to black (positive values).

and takes on large absolute values in the thermal boundary layers and on the borders of the thermal plumes.

Mean characteristics for ϵ_θ and $C(T, \epsilon_\theta)$ can be obtained by multiplication of the energy equation (2) with any function η and further time and volume averaging. Taking $\eta = T$ we get the mean thermal dissipation rate

$$\langle \epsilon_\theta \rangle_{t,V} = \Gamma^{1/2} Ra^{-1/2} Pr^{-1/2} Nu,$$

where $\langle \cdot \rangle_{t,V}$ denotes time and volume averaging and Nu is the Nusselt number (5), while $\eta = T^2$ gives $\langle C(T, \epsilon_\theta) \rangle_{t,V} = 0$.

6. Volume of the thermal boundary and interior layers and their contribution to heat transport

Since the boundary and interior layers in contrast to the turbulent background are indicated by large values of the thermal dissipation rate, analysing the spatial distribution of ϵ_θ one can investigate volume characteristics of these large coherent structures and the turbulent background and study separately their contributions to the volume averaged thermal dissipation rate.

In [10] two functions, $\tau(\xi)$ and $\sigma(\xi)$, were introduced and evaluated from the DNS data to investigate quantitatively the role of the turbulent background. The function $\tau(\xi)$ describes the percentage of the fluid volume, for which the thermal dissipation rate does not exceed $\xi \times 100\%$ of its maximum value $\epsilon_{\theta,\max} = \max_V \epsilon_\theta$,

$$\tau(\xi) = \langle \vartheta(\xi \epsilon_{\theta,\max} - \epsilon_\theta) \rangle_V, \quad (8)$$

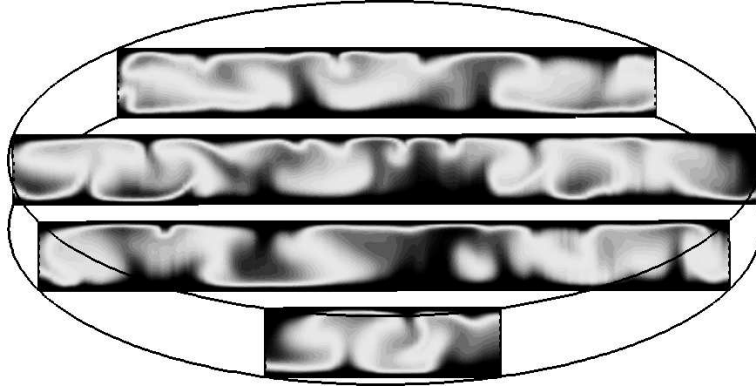


Figure 5: Snapshots of the temperature for $Ra = 10^5$, $\Gamma = 10$ in vertical cross-sections. Colour scale spreads from white (zero) to black (large absolute values).

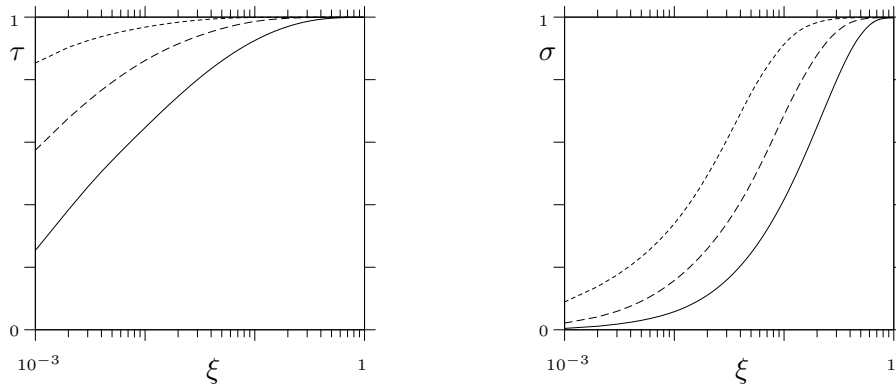


Figure 6: Portion of the domain, where $\epsilon_\theta(\mathbf{x}) \leq \xi \epsilon_{\theta, \max}$ (left) and contribution to the volume averaged thermal dissipation rate from the parts of the domain, where $\epsilon_\theta(\mathbf{x}) \leq \xi \epsilon_{\theta, \max}$ (right), evaluated in the DNS for $Ra = 10^5$ (—), $Ra = 10^6$ (---) and $Ra = 10^7$ (- - -) and $\Gamma = 10$.

and $\sigma(\xi)$ describes the contribution to the volume-averaged thermal dissipation rate from those parts of the domain, where ϵ_θ does not exceed $\xi \times 100\%$ of its maximum,

$$\sigma(\xi) = \frac{\langle \epsilon_\theta \vartheta(\xi \epsilon_{\theta, \max} - \epsilon_\theta) \rangle_V}{\langle \epsilon_\theta \rangle_V}. \quad (9)$$

Here $\vartheta(x)$ is the Heaviside function, $\vartheta(x) = 1$, if $x \geq 0$ and $\vartheta(x) = 0$ otherwise.

In Fig. 6 (a) and (b), respectively, the functions $\tau(\xi)$ and $\sigma(\xi)$ are plotted for $Ra = 10^5$, 10^6 and 10^7 and $\Gamma = 10$. Taking into account the fact that for any fixed value of ξ the values of $\tau(\xi)$ and $\sigma(\xi)$ obtained for a certain Rayleigh number are always higher than the corresponding values for a lower Rayleigh number, we conclude that both, the portion of the whole domain, which corresponds to relatively small values of the thermal dissipation rate, and the contribution to the volume-averaged thermal dissipation rate from these parts of the domain, increase with the Ra . In another words, the contribution of the turbulent background in both cases increases with growth of the Rayleigh number and the contribution of the thermal layers decreases with Ra . This supports the conjecture by Grossmann and Lohse [20] about the dominating role of the turbulent background in RBC with large Rayleigh numbers.

References

- [1] G. Ahlers, "Experiments with Rayleigh-Bénard Convection", *In: Dynamics of spatiotemporal structures - Henri Benard centenary review (Ed. Mutabazi, I., Guyon, E. & Wesfreid,*

- J.E.*), *Springer Tracts in Modern Physics* (2005).
- [2] E. D. Siggia, "High Rayleigh number convection", *Ann. Rev. Fluid Mech.*, **26**, 137–168 (1994).
 - [3] S. W. Morris, E. Bodenschatz, D. S. Cannell & G. Ahlers, "Spiral defect chaos in large aspect ratio Rayleigh–Bénard convection", *Phys. Rev. Lett.*, **71**, 2026–2029 (1993).
 - [4] M. Assenheimer & V. Steinberg, "Observation of coexisting upflow and downflow hexagons in Boussinesq Rayleigh–Bénard convection", *Phys. Rev. Lett.*, **76**, 756–759 (1996).
 - [5] A. V. Getling, "Rayleigh–Bénard convection", *World Scientific* (1998).
 - [6] F. H. Busse, "Spoke pattern convection" *Acta Mechanica Suppl.*, **4**, 11–17 (1994).
 - [7] H.-D. Xi, S. Lam & K.-Q. Xia, "From laminar plumes to organized flows: the onset of large-scale circulation in turbulent thermal convection", *J. Fluid Mech.*, **503**, 47–56 (2004).
 - [8] A. Leonard & G. S. Winckelmans. "A tensor-diffusivity subgrid model for Large-Eddy Simulation", *Caltech ASCI technical report, cit-asci-tr043*, 043 (1999).
 - [9] O. Shishkina & C. Wagner, "A fourth order accurate finite volume scheme for numerical simulations of turbulent Rayleigh–Bénard convection", *C.R. Mecanique*, **333**, 17–28 (2005).
 - [10] O. Shishkina & C. Wagner, "Analysis of thermal dissipation rates in turbulent Rayleigh–Bénard convection", *J. Fluid Mech.*, **546**, 51–60 (2006).
 - [11] G. Grötzbach, "Spatial resolution requirements for direct numerical simulation of Rayleigh–Bénard convection", *J. Comput. Phys.*, **49**, 241–264 (1983).
 - [12] R. Verzicco & R. Camussi, "Numerical experiments on strongly turbulent thermal convection in a slender cylindrical cell". *J. Fluid Mech.*, **477**, 19–49 (2003).
 - [13] N. S. Bakhvalov, "Towards optimization of methods for solving boundary value problems in the presence of a boundary layer", *Zh. Vychisl. Mat. Mat. Fiz.*, **9**, 841–859 (1969).
 - [14] G. I. Shishkin, "On finite difference fitted schemes for singularly perturbed boundary value problems with a parabolic boundary layer", *J. Math. Anal. Appl.*, **208**, 181–204 (1997).
 - [15] Y. Qiu & D. M. Sloan, "Analysis of difference approximations to a singularly perturbed two-point boundary value problem on a adaptively generated grid", *J. Comput. Appl. Math.*, **101**, 1–25 (1999).
 - [16] N. Kopteva & M. Stynes, "A robust adaptive method for a quasilinear one-dimensional convection-diffusion problem", *SIAM J. Numer. Anal.*, **39**, 1446–1467 (2001).
 - [17] R.E. Bank & A. Weiser, "Some a posteriori error estimates for elliptic partial differential equations", *Math. Comput.*, **44**, 283–301 (1985).
 - [18] E.S. Nikolaev & O.V. Shishkina, "Method of solving the Dirichlet problem for the 2nd order elliptic equations in polygonal domain on adaptive refining meshes sequence", *Mosc. Univ. Comput. Math. Cybern.*, **4**, 3–15 (2005).
 - [19] J. F. Thompson, "Numerical grid generation", *Elsevier Science Publishing*, 305–310 (1985).
 - [20] S. Grossmann & D. Lohse, "Scaling in thermal convection: a unifying theory", *J. Fluid Mech.*, **407**, 27–56 (2000).